Check for updates

Impact-driven mobilization of deep crustal brines on dwarf planet Ceres

C. A. Raymond[1 ✉], A. I. Ermakov[1,2], J. C. Castillo-Rogez[1], S. Marchi[3], B. C. Johnson[4], M. A. Hesse[5], J. E. C. Scully[1], D. L. Buczkowski[6], H. G. Sizemore[7], P. M. Schenk[8], A. Nathues[9], R. S. Park[1], T. H. Prettyman[7], L. C. Quick[10], J. T. Keane[1,11], M. D. Rayman[1] and C. T. Russell[12]

Ceres, the only dwarf planet in the inner Solar System, appears to be a relict ocean world. Data collected by NASA's Dawn spacecraft provided evidence that global aqueous alteration within Ceres resulted in a chemically evolved body that remains volatile-rich[1]. Recent emplacement of bright deposits sourced from brines attests to Ceres being a persistently geologically active world[2,3], but the surprising longevity of this activity at the 92-km Occator crater has yet to be explained. Here, we use new high-resolution Dawn gravity data to study the subsurface architecture of the region surrounding Occator crater, which hosts extensive young bright carbonate deposits (faculae). Gravity data and thermal modelling imply an extensive deep brine reservoir beneath Occator, which we argue could have been mobilized by the heating and deep fracturing associated with the Occator impact, leading to long-lived extrusion of brines and formation of the faculae. Moreover, we find that pre-existing tectonic cracks may provide pathways for deep brines to migrate within the crust, extending the regions affected by impacts and creating compositional heterogeneity. The long-lived hydrological system resulting from the impact might also occur for large impacts in icy moons, with implications for creation of transient habitable niches over time.

Compositional, geological and geophysical observations returned during Dawn's prime mission found a globally homogeneous surface composition and partially differentiated interior for Ceres[1,4,5]. They also revealed heterogeneities on regional scales[6] and local bright deposits (faculae) enriched in carbonates and salts. While faculae occur globally on Ceres, particularly in association with young craters[7,8], Occator crater has the brightest, most well-preserved deposits. To better understand the contribution of impacts to the evolution of Ceres's crust, the final phase of the Dawn mission (second extended mission, XM2) was designed to investigate the ~20-Myr-old Occator crater[2] at a spatial resolution ten times better than achieved during the prime mission. In XM2, the spacecraft achieved a minimum altitude below 35 km over Occator crater (20° N, 120° W), imaging most of the crater at resolution of 3.3–10 m pixel⁻¹, and increasing spatial sampling of all other instruments. In particular, it yielded gravity variations[9] at the scale of the geological units of the crater itself and surrounding areas. The XM2 data elucidate the interaction of the impactor with the ice-rich crust, and the processes by which brine deposits formed within the crater[2,10,11].

Occator crater is located within Hanami Planum, a discrete highland of ~555 km diameter with elevation reaching 6 km (ref. [12]) (Fig. 1a). Density heterogeneities in the region are probed by computing isostatic gravity anomalies, which are anomalies that remain after accounting for assumed compensated topography (see Methods). The authors of ref. [13] derived a mean crustal density of 1,287 kg m⁻³, mean mantle density of 2,434 kg m⁻³ and mean crustal thickness of 41.0 km for a two-layer model that minimized the global admittance misfit under the assumption that the observed gravitational moment J_2 is hydrostatic to within 3%. The isostatic anomaly map of Hanami Planum shows a distinctive broad-scale negative gravity anomaly that is anti-correlated with topography[13] (Extended Data Fig. 1), indicating substantial heterogeneity relative to surrounding areas. Even after removing the long-wavelength ($n < 3$) field, the isostatic gravity map for the region displays predominantly negative anomalies (Fig. 1b), indicating excess lighter material relative to Ceres's average density profile. The high-resolution XM2 gravity data resolve localized (to 37–50 km) anomalies within a portion of Occator crater, and in the adjacent regions (Extended Data Fig. 2), including the largest negative anomaly observed on Ceres (<−95 mGal) located southeast of the crater at ~12° N, 113° W (Fig. 1b). These new gravity data allow testing of hypotheses based on lower-resolution prime mission data regarding the relative roles of impact heating and pre-existing heterogeneities in creating subsurface brine reservoirs that sourced the Occator crater bright deposits. More broadly, the improved resolution in this sector reveals details of the crustal density structure that links large-scale and impact-induced fracturing to brine mobility.

The −50 to −70 mGal isostatic anomaly within Occator crater itself cannot be attributed solely to ice-rich lobate flow deposits found on the crater floor, because these deposits are too thin[10,11] to account for the observed gravity signature. Instead, the asymmetry of the gravity low relative to the crater, and the fact that it merges with the larger negative anomaly to the southeast suggest it may be influenced by regional crustal structure. The ~80-km-diameter

[1]Jet Propulsion Laboratory, California Institute of Technology, Pasadena, CA, USA. [2]University of California, Berkeley, Berkeley, CA, USA. [3]Southwest Research Institute, Boulder, CO, USA. [4]Purdue University, West Lafayette, IN, USA. [5]University of Texas, Austin, TX, USA. [6]Johns Hopkins University Applied Physics Laboratory, Laurel, MD, USA. [7]Planetary Science Institute, Tucson, AZ, USA. [8]Lunar and Planetary Institute, Houston, TX, USA. [9]Max Planck Institute for Solar System Research, Goettingen, Germany. [10]NASA Goddard Space Flight Center, Greenbelt, MD, USA. [11]Division of Geology and Planetary Sciences, California Institute of Technology, Pasadena, CA, USA. [12]University of California, Los Angeles, Los Angeles, CA, USA. ✉e-mail: Carol.A.Raymond@JPL.NASA.gov
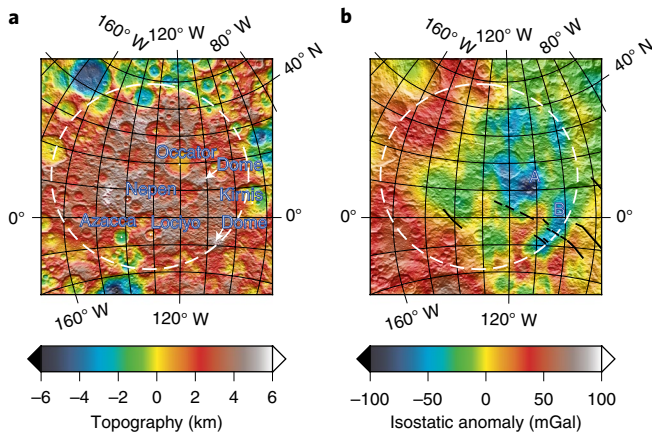
Fig. 1 | Topography and isostatic gravity of the Hanami Planum region (dashed white line). a, Topography plotted relative to the geoid. The four youngest craters in Hanami Planum—Occator, Azacca, Lociyo and Nepen—are annotated, as is an older crater, Kirnis, which hosts a large dome. **b**, Isostatic gravity map showing the field up to degree strength (Extended Data Fig. 2), with the low-degree (n < 3) field removed. The largest and best-resolved negative isostatic anomalies that are annotated A and B are associated with domes marked in **a**, while another negative anomaly north of Occator is associated with a flat topographic high, but has no other distinguishing features. The Samhain Catenae[16] are indicated by black lines. Although not resolved at highest resolution in the gravity field, the topographic high that hosts Nepen crater has a local negative isostatic gravity anomaly.

heterogeneities. Two models were run: the first sought the source of the broad negative anomaly that spans Hanami Planum, and the second attempted to discern the source of the discrete negative anomaly A southeast of Occator (see Methods). Results are reported in Extended Data Table 1, along with the constraints for the two models in Extended Data Tables 2 and 3. Posterior distributions are shown in Extended Data Figs. 3 and 4. The total mass deficits and the positions of the source centres are tightly bounded, while other parameters are poorly constrained. Hanami Planum's total mass deficit was found to be ~0.1% of Ceres's mass ($97.1^{+1.6}_{-1.5} \times 10^{16}$ kg), and the Occator region's residual mass deficit is >10 times smaller than Hanami Planum's ($7.5^{+0.6}_{-0.6} \times 10^{16}$ kg). Modelling results point to a deep-mantle source for the broad Hanami Planum anomaly (Fig. 2a and Extended Data Fig. 3). Its density contrast of 30–70 kg m^{-3} (Extended Data Fig. 3) implies a deep-seated heterogeneity that may be evidence for chemical and/or thermal convection in a mud mantle[24]. Alternatively, a simple explanation is that the thicker, low-conductivity crust in the Hanami region resulted in a higher mantle temperature relative to the surroundings. The warmer mantle temperature would result in a higher degree of brine–silicate differentiation, leading to a higher brine concentration (and lower density) in the mid-to-upper mantle beneath Hanami, as evidenced from the MCMC density inversion. An increase of only a few per cent in the brine fraction can account for the density anomaly. Residual isostatic anomaly fields were calculated by removing a median density contrast as specified in Extended Data Fig. 4. The inferred source of the broad Hanami Planum anomaly only removes the long-wavelength low (Fig. 2c), yielding residual anomalies similar to the n > 3 field in Fig. 1b. It does not account for the local negative isostatic anomalies associated with the region surrounding Occator (Fig. 2e).

The inferred position and extent of the source near Occator crater suggests a low-density region in the lower crust and upper mantle (Fig. 2b), centred outside the crater but overlapping its southeast quadrant. The residual isostatic anomalies shown in Fig. 2f are reduced relative to those of the larger Hanami Planum source (Fig. 2e), supporting the existence of this discrete additional source. The source near Occator crater partially overlaps the solution space for the broad and deep Hanami Planum anomaly source, which could indicate that these source regions are connected. The density deficit in this mid-to-sub crustal region (45–200 kg m^{-3}) is consistent with brine enrichment. This inferred brine-rich region likely contributed to prolonged eruptions within Occator crater facilitated by fracture networks. After subtracting a representative MCMC model solution for the Occator area (Fig. 2d and Extended Data Table 4), a negative anomaly remains centred over the dome associated with anomaly A (Fig. 2f), which is consistent with a localized low-density intrusion into the shallow crust. The previously discussed association of negative isostatic anomalies with domes and fractures in Hanami Planum suggests that multiple intrusions into the shallow crust may have been fed by similar discrete lower crustal brine reservoirs via pre-existing and impact-induced fractures, and possibly fed by the deep source beneath Hanami Planum. In addition, the presence of this inferred brine-enriched region beneath the southeastern portion of Occator crater could have fed eruptions at the Vinalia Faculae via the fracture network.

anomaly southeast of the crater (A in Fig. 1b) is associated with a 70 × 30 km dome, rising 2–3 km above the background, and lies in a highly fractured region within the Occator ejecta blanket[14,15]. This anomaly and dome straddle a linear feature that aligns with one splay of the Samhain Catenae, a set of deep pit chains inferred to be the surface expression of primordial fractures penetrating deep into the crust[16]. Another isostatic gravity low crosses the Samhain Catenae and a large dome within Kirnis crater (B in Fig. 1b)[14,17], and a >2-km-high, 50-km-wide dome defines its southwestern end. Large, globally distributed domes including Cerealia Tholus (tens of kilometres wide with kilometres of relief)[17] are thought to have formed by cryovolcanism[17–20] or ice diapirism[21]. The prime mission gravity data do not resolve the gravity signatures of these domes, except for Ahuna Mons, which has a large positive anomaly thought to be the result of extrusion of a mud-rich slurry[22]. In contrast, XM2 isostatic gravity data do resolve the signatures of domes at Hanami and their negative anomalies indicate that they are composed of low-density material. The proximity of the Hanami domes to large fractures is consistent with fractures providing conduits to move low-density brines into the shallow crust. The depths of young craters in Hanami Planum—Occator, Azacca, Lociyo and Nepen—are also shallower than expected, and fracture patterns on their floors are consistent with uplift by intrusions[14]. The inferred presence of mobile brines beneath Hanami Planum indicated by morphology and gravity supports the prediction of warmer temperatures in the sub-Hanami crust and mantle, which is attributed to lower thermal conductivity resulting from thicker crust and preservation of a large fraction of its original clathrate hydrate content[23].

To constrain the sources of isostatic anomalies beneath Hanami Planum, a Markov chain Monte Carlo (MCMC) approach was used to invert the gravity field, producing probability distributions for the positions and dimensions of biaxial ellipsoidal sources. These ellipsoidal sources simplify the likely complex density structure to allow efficient computation of the location and magnitude of density

To understand the interaction of the Occator impact with the underlying brine-rich region, hydrocode modelling of impact heating[25] and thermal modelling of the evolution of the resulting melt chamber under varying assumptions for thermal conductivity[23,26] were investigated to understand melt chamber geometry and lifetime (see Methods, and Extended Data Figs. 5a and 6). For an assumed thermal conductivity consistent with 50 vol% clathrate hydrate content in the crust[23], the initial melt chamber ($T > 245$ K brine eutectic) would have formed a column roughly 24 km in diameter that merged with a persistent deep crustal brine layer at ~35 km depth (Fig. 3). This mod-
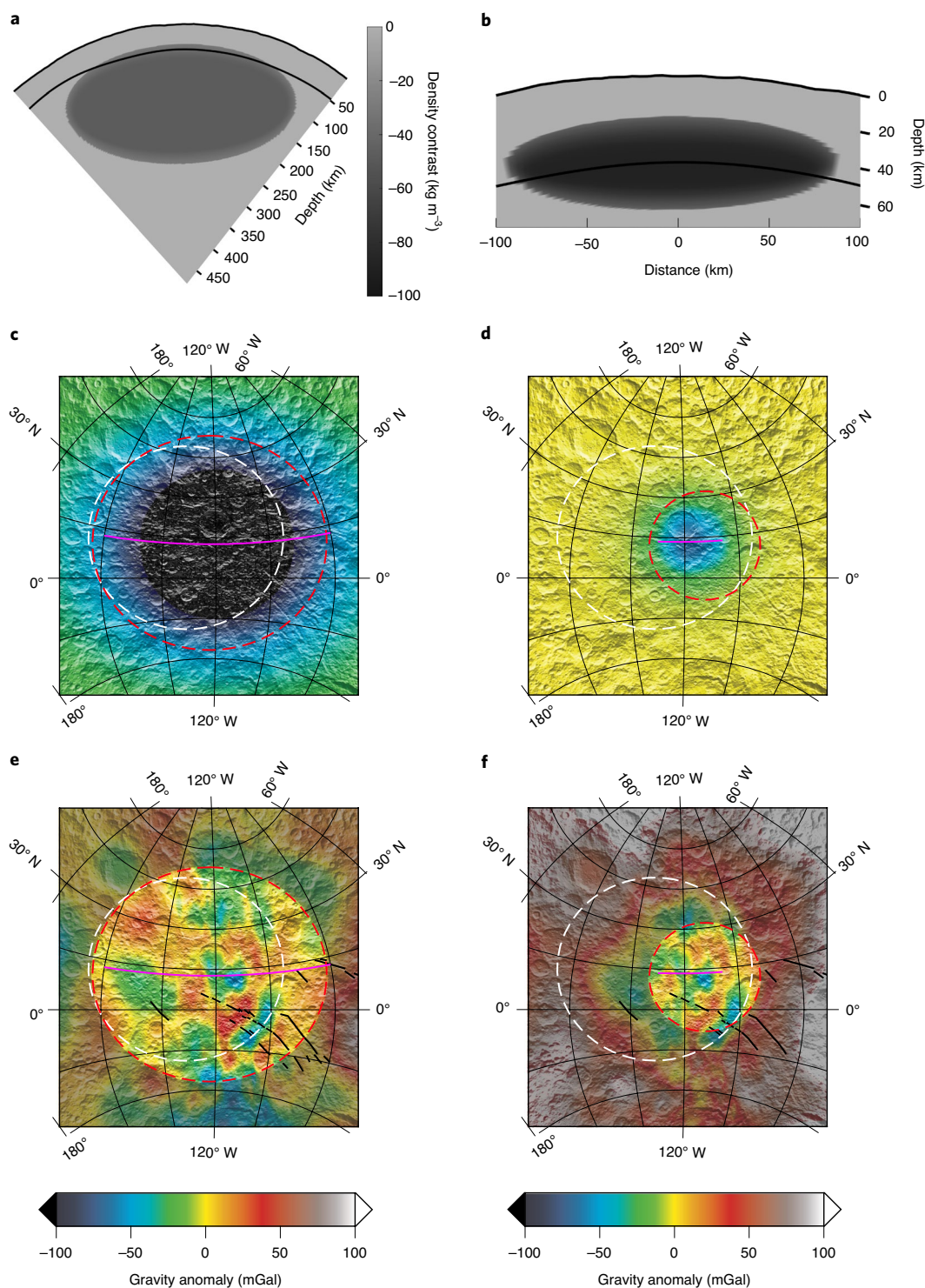
Fig. 2 | Cross-sections of biaxial ellipsoids showing representative low-density regions in the Hanami Planum region and in the local area around Occator crater consistent with the gravity inversion, and their gravity signatures. a–f, Cross-sections of median density contrast were computed (see Methods) at 12.7° N latitude between longitudes 80.0° W and 160.0° W for the broad-scale Hanami Planum anomaly (**a**), and for 100 km east and west of longitude 118.0° W at latitude 13.5° N for anomaly A (**b**). Solid black lines in **a** and **b** represent the surface and the crust/mantle boundary at a depth of ~50 km (ref. [13]), under the assumption that it is isostatic. Gravity acceleration for these representative high-likelihood (not best-fit) ellipsoidal models for Hanami Planum and anomaly A are shown in **c** and **d**, respectively. In **c–f**, the outline of Hanami Planum is shown by the dashed white circle, the solution region for each gravity inversion is shown by a red dashed circle and the location of the cross-sections shown in **a** and **b** are shown by the magenta curves. Parameters of these models are given in Extended Data Table 4. Residual gravity anomalies that remain after subtracting the modelled gravity fields from the isostatic anomaly field are shown in **e** and **f**. Prior to inversion of the anomaly A region (**f**), the mean value of the isostatic gravity anomaly within an annulus with inner radius of 20° and outer radius of 30°, centred at 113° W and 12° N, was subtracted to isolate the effect of the local anomaly to the southeast of Occator crater; residuals in the shaded area outside the dashed red circle in **e** and **f** are not meaningful. Subtracting the local field obtained for the anomaly A inversion effectively reduces the amplitude of the local isostatic anomalies; residuals suggest remaining density variability at small spatial scales.
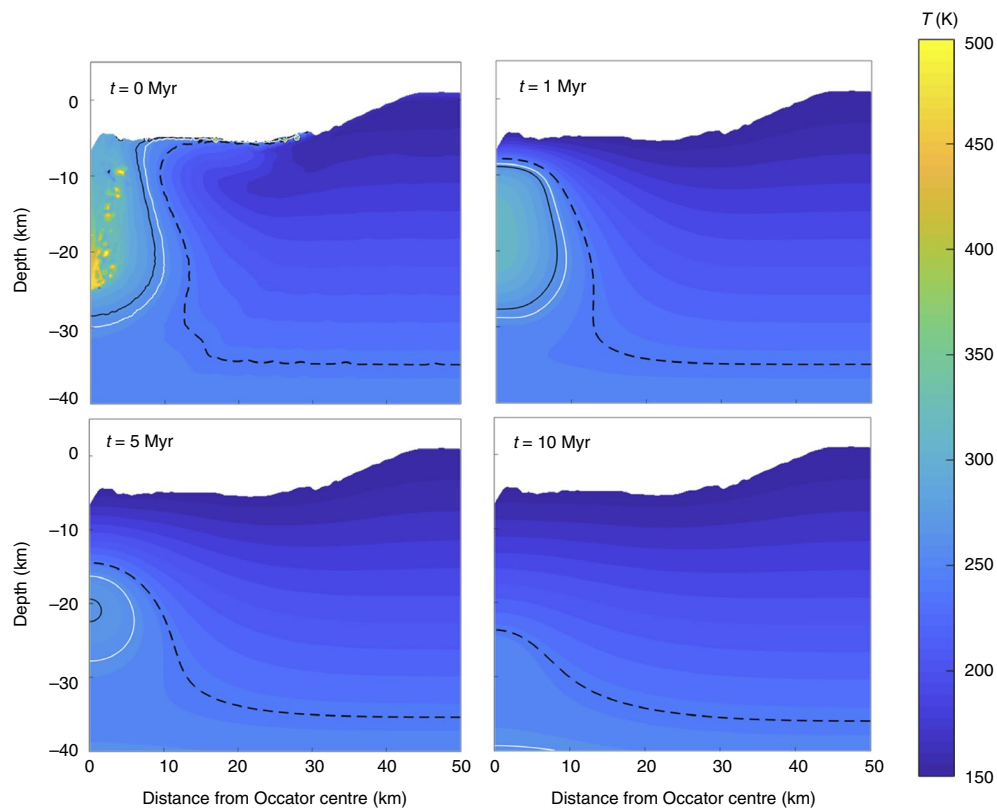
Fig. 3 | Evolution of the temperature field in Occator crater at t = 0, 1, 5 and 10 Myr after the crater-forming impact. The starting model is the temperature field from the iSALE simulation of ref. [25], scaled for a higher thermal gradient of 2.73 K km^{-1} (see Methods). The black curve marks the 273 K isotherm corresponding to the water eutectic, inside which the material is fully molten (magma chamber). The dashed black curve marks the 245 K isotherm corresponding to the ammonium chloride eutectic, marking the boundary of partially molten material. The white curve marks the 265 K isotherm, inside which sodium carbonate is in solution.

elling shows that the impact-produced thermal anomaly persists at depth for >10 Myr post-impact. The predicted impact damage region (Extended Data Fig. 5b) shows fractures extending to tens of kilometres beyond the crater rim and intersecting the predicted persistent brine layer. Impact fracturing would connect the impact melt chamber with the deeper brine-rich layer, as well as the brine-rich region identified in the gravity inversion. Prolonged freezing of the impact melt chamber and continued supply of brine from depth through the fracture network can explain the ~20 Myr discrepancy between the age of the crater and the time of the most recent intrusion[2], as well as evidence for ongoing activity[27]. It also allows time for chemical evolution of the brines, for example by interaction with regolith and impactor material embedded in the melt chamber[23,28].

This work lends observational constraints to support the evolutionary framework inferred from Dawn's prime mission data, and provides context for other XM2 observations[2,10,11]. In particular, it resolves the debate on the origin of the faculae and shows that the two models previously introduced (impact melt chamber and deep brine reservoirs) act jointly to explain long-lived brine effusion. In the resulting evolutionary scenario synthesized in Fig. 4, the initially water-rich impact-produced melt chamber froze from the top down in about 5 Myr (Fig. 3), becoming increasingly salt-rich. Pressure from gas release and volume changes drove brines from the deep crustal region to the surface through reactivated fractures until the pressure subsided, the brine conduits froze, and the cycle started anew[20,29]. Such pressure-driven cryovolcanic eruptions have also been suggested for Europa[30]. Later-erupting brines created the sodium-carbonate-rich Cerealia Tholus in the central pit, and the Vinalia Faculae along fractures in the crater floor[10,11,20,31]. Our

observations suggest that the Vinalia Faculae were sourced from the crustal brine-rich region underlying the southeastern portion of the crater. Cerealia Tholus, the 600-m dome in the centre of Cerealia Facula, appears to be the most recent stage of this system[15,31,32], where brines rich in NH$_4$Cl and containing hydrohalite erupted through radial extensional fractures[2,27,32].

Ceres's history as revealed by Dawn provides an exemplar for understanding the evolution of icy bodies that partially or completely differentiated. The deep compositional heterogeneity inferred from its density structure, which may reflect interior convection or regional variations in mantle temperature and brine content, may be applicable to other bodies with mostly frozen silicate-rich interiors, such as Charon. The role of impacts in mobilizing oceanic materials that spill onto the surface has been demonstrated for this dwarf planet that bears many similarities to icy moons, indicating that large impacts in icy shells, especially if they are relatively thin (a few tens of kilometres, such as Europa), could connect a subsurface ocean to a local melt chamber. In addition, injection of ocean material into impact-induced fractures could generate crustal heterogeneities in any body that had an ocean phase during its evolution. Impact simulations[25] indicate a substantial fraction of the impactor may be retained in the melt chamber. The geochemical characteristics of the resulting reservoir, which combines a crustal component, oceanic component and exogenic material, could have important implications for astrobiology[28]. Comparison with data returned by the upcoming Europa Clipper and Jupiter Icy Moons Explorer (JUICE) missions will further our understanding of the role of impact-produced heat and damage in driving local geological activity and introducing heterogeneities in icy crusts.
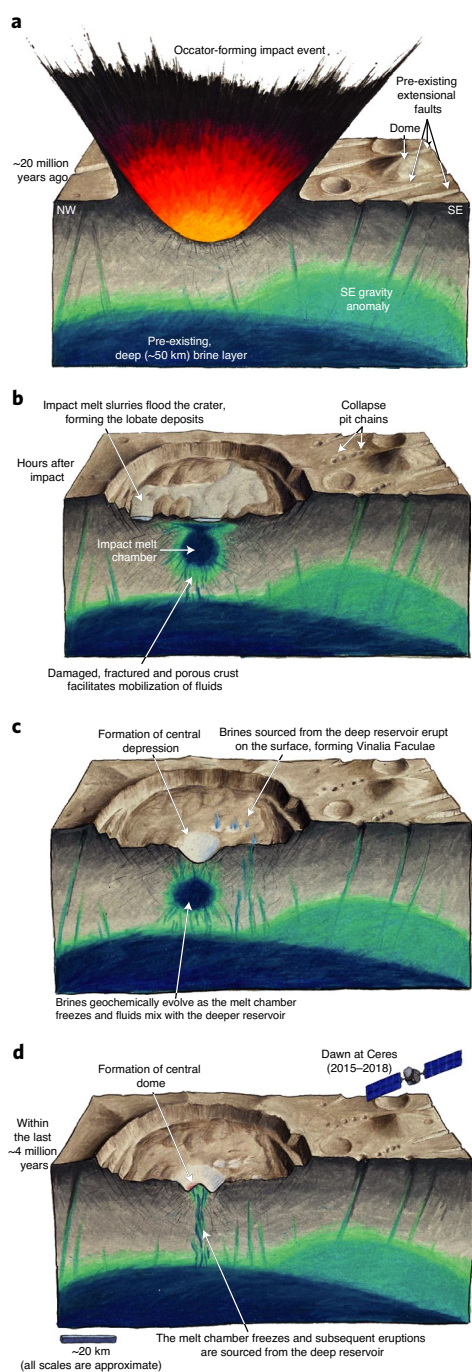
Fig. 4 | Evolution of the melt chamber beneath Occator and scenario of brine emplacements. a, Impact occurs at ~20 Myr (ref. [2]). **b**, Impact slurries flood the crater floor immediately following impact[10,11], consistent with hydrocode models[25] that predict a large water-rich melt chamber. **c**, As the impact melt chamber freezes from the top down and mixes with the deep brine reservoir, chemically evolved brines are periodically erupted under pressure, forming the faculae. **d**, In the final stage (~4 Myr), Cerealia Tholus forms within Cerealia Facula, erupting brines sourced from the deep reservoir. The morphology and colour variations on the dome, as well as the presence of metastable hydrohalite[27] attest to its relative youth[2,32]. SE, southeast; NW, northwest. Credit: J. T. Keane, NASA/Caltech JPL.

Methods

Isostatic gravity anomaly. Analysis of Ceres's gravity[33] and topography[34] showed that their spectral characteristics are consistent with a decrease in viscosity with

depth in the upper 100 km of Ceres[35]. Therefore, the crust of Ceres is expected to be isostatically compensated such that topographic highs are supported by displacements of a higher-density mantle[4,13]. In this study, the isostatic gravity anomalies were computed based on a viscous flow model. In such a model, the viscous relaxation of an arbitrary top load for a two-layer spherical body is computed via the propagator matrix approach[36]. The inner (mantle) layer is inviscid and the upper (crustal) layer is assumed to have a uniform density and viscosity. The isostatic gravity anomaly is defined as the difference between the observed gravity and the modelled isostatic gravity. Degree 1 was assumed to be uncompensated. The difference between the isostatic anomalies computed with the viscous flow model and the equal pressure isostasy model[37] reaches 15 mGal and does not affect the interpretation of the features discussed in this work. A detailed description about the assumptions and models used for computing the isostatic anomaly can be found in the Methods section of ref. [9] and in the Appendix of ref. [13].

Density inversions with MCMC. The gravity field was determined up to degree 70 along with the covariance matrix of the gravity coefficients. The gravity effective resolution is spatially variable. The degree strength[38] is determined as the maximum degree at which the power of the gravity signal is equal to the power of the noise and thus serves as a measure of effective resolution. Extended Data Fig. 1 is computed by evaluating the gravity field up to local degree-strength. To characterize the errors in the gravity field coefficients, we sampled the covariance matrix to generate sets of gravity field clones. The variance in the radial gravitational acceleration at latitude ϕ and longitude λ is then found as:

$$\sigma_g^2(\lambda, \phi) = \frac{1}{n-1} \sum_{i=1}^{n} (g_i(\lambda, \phi) - \bar{g}_{\mathrm{obs}}(\lambda, \phi))^2 \qquad (1)$$

where n is the number of clone fields, $g_i(\lambda,\phi)$ is the value of the radial gravity computed from the ith gravity clone and $\bar{g}$ is the mean value of the radial gravity.

We used the MCMC method[39,40] to fit the gravity created by a mascon to the observed gravity field. The source of the anomaly is assumed to be a biaxial ellipsoid one of whose axes is aligned with the radial direction. Thus, a mascon model can be defined by six parameters in total: three coordinates of the ellipsoid centre, two ellipsoidal semiaxes and density contrast. The gravity field created by an anomalous ellipsoid was first computed analytically[41], and then expanded in spherical harmonics in the same way as the observed gravity field, that is, up to the same spatially variable degree strength. We used the publicly available Python library emcee that employs ensemble sampler with affine invariance. A full description of this method is given in ref. [42]. The log-likelihood function was taken to be:

$$\ln L = -\frac{1}{2} \sum_{i=1}^{n} \frac{(\Delta g_{\mathrm{mod}}(\lambda, \phi) - \Delta g_{\mathrm{isostatic}}(\lambda, \phi))^2}{\sigma_g^2(\lambda, \phi)}, \qquad (2)$$

where $\Delta g_{\mathrm{isostatic}}$ is the isostatic anomaly derived from the observations[4,14] and Δg_{mod} is the model gravity anomaly. We performed two MCMC runs to explore the parameter space of (1) the broad Hanami Planum negative isostatic anomaly and (2) the strong and localized negative isostatic anomaly to the southeast of Occator crater. The parameter bounds for the Hanami Planum and Occator southeast anomaly runs are given in Extended Data Tables 2 and 3, respectively. The prior probability distribution of the model parameters was assumed uniform within the bounds. For Hanami Planum runs, we used the entire isostatic anomaly field computed from degree 1 to local degree-strength as an input. For the Occator southeast runs, in order to isolate the local negative signal, we subtracted the average isostatic anomaly within an annulus centred at 113° W and 12° N with an inner radius of 20° and outer radius of 30°.

The posterior distributions of the model parameters are presented in the triangle plots (Extended Data Figs. 3 and 4) that show two-dimensional histograms of each parameter pair. One-dimensional histograms of each parameter are also shown on the top. These plots illustrate the trade-offs between parameters. While position and mass deficits are well constrained, ellipsoid dimensions range over factors of two, and associated density contrasts are poorly constrained, ranging from 10 to >100 kg m^{-3} in absolute value.

To compute the median density contrasts shown in Fig. 2, histograms of density contrasts were built pointwise on the cross-sections using the chains of parameter values resulting from MCMC runs, then the median value of density contrast was computed from those histograms. The resulting median density field does not represent a density distribution that best reproduces the gravity observations. Rather, it serves as a visualization of the anomaly's median location and density contrast.

Extrapolation of iSALE simulation to variable thermal gradients. Previously, formation of Occator was simulated assuming a linear thermal gradient of 0.5 K km^{-1} from a surface temperature of 150 K (ref. [25]), using the iSALE-2D shock physics code[43,44]. However, the regional thermal gradient is expected to be higher than that (2.11 to 2.73 K km^{-1}) as derived by thermal modelling described below. Here we scale the temperature results of ref. [25] to account for these higher thermal gradients assuming the final distribution of material within the crater is the

same as reported by ref. [25]. We extracted the final temperature, T_0, of Lagrangian tracer particles from the preferred simulation of ref. [25], which is the formation of an Occator-like crater in an ice–rock mixture composed of 30% ice by mass. Lagrangian tracer particles track the motion of a parcel of material and thus record the initial or provenance depth of material, d_0. We then found the new temperature of each tracer according to $T_{new} = T_0 + d_0 \left(\frac{dT}{dz} - 0.5\,\text{K km}^{-1} \right)$, where $\frac{dT}{dz}$ is the newly assumed thermal gradient. The damage distribution cannot be scaled according to temperature easily. However, the fracturing happens at a high strain rate such that nearly all of Ceres should behave elastically during the impact event.

Thermal modelling for Hanami Planum. Modelling of the temperature profile at Hanami Planum is based on the one-dimensional conductive heat transfer model by ref. [23]. That study assumed an average interior structure for Ceres (40 km crust). The model developed for this study is tailored for Hanami Planum and assumes a 55-km-thick crust. The model also assumes 50 vol% clathrate hydrates under the assumption that the region of Hanami Planum has been spared from massive impacting, in contrast to the surrounding basins (for example, Vendimia Planitia)[45]. The new model calculation for 50 vol% clathrate hydrates shows a temperature at the base of the crust of 273 K at present in Extended Data Fig. 6. Since the ~15 km lower part of the crust is at/above the eutectic temperatures of the bulk of the salt compounds in Ceres[46], that region is partially molten. Lateral variations in crustal thickness produce very different temperatures at the base of the crust. Below the ~30-km-thick crust in the basin areas, the temperature is closer to the eutectic temperature of chloride mixtures (~220 K), which allows for ~0.3% melt[46].

Data availability

The data that support the plots within this paper, and conclusions of this study are available from the PDS Small Bodies Node website (https://sbn.psi.edu/pds/resource/dawn) or from the corresponding author upon reasonable request.

References

1. Ammannito, E. et al. Distribution of ammoniated magnesium phyllosilicates on Ceres. *Science* **353**, aaf4279 (2016).
2. Nathues, A. et al. Recent cryovolcanic activity at Occator crater on Ceres. *Nat. Astron.* https://doi.org/10.1038/s41550-020-1146-8 (2020).
3. De Sanctis, M. C. et al. Bright carbonate deposits as evidence of aqueous alteration on on (1) Ceres. *Nature* **536**, 54–57 (2016).
4. Park, R. S. et al. Interior structure of dwarf planet Ceres from measured gravity and shape. *Nature* **537**, 515–517 (2016).
5. Prettyman, T. H. et al. Extensive water ice within Ceres' aqueously altered regolith: evidence from nuclear spectroscopy. *Science* **355**, 55–59 (2017).
6. Williams, D. A. et al. Introduction: the geologic mapping of Ceres. *Icarus* **316**, 1–13 (2018).
7. Stein, N. T. et al. The formation and evolution of bright spots on Ceres. *Icarus* **320**, 188–201 (2017).
8. Carrozzo, F. G. et al. Nature, formation, and distribution of carbonates on Ceres. *Sci. Adv.* **4**, e1701645 (2018).
9. Park, R. S. et al. Evidence of non-uniform crust of Ceres from Dawn's high-resolution gravity data. *Nat. Astron.* https://doi.org/10.1038/s41550-020-1019-1 (2020).
10. Scully, J. E. C. et al. Formation of the bright faculae in Ceres' Occator crater via long-lived brine effusion in a hydrothermal system. *Nat. Commun.* https://doi.org/10.1038/s41467-020-15973-8 (2020).
11. Schenk, P. et al. Impact heat driven volatile redistribution at Occator, Ceres, as a comparative process. *Nat. Commun.* https://doi.org/10.1038/s41467-020-17184-7 (2020).
12. Buczkowski, D. L. et al. The geomorphology of Ceres. *Science* **353**, aaf4332 (2016).
13. Ermakov, A. I. et al. Constraints on Ceres' internal structure and evolution from its shape and gravity measured by the Dawn spacecraft. *J. Geophys. Res.* **122**, 2267–2293 (2017).
14. Buczkowski, D. L. et al. The geology of the Occator quadrangle of dwarf planet Ceres: floor-fractured craters and other geomorphic evidence of cryomagmatism. *Icarus* **316**, 128–139 (2018).
15. Scully, J. E. C. et al. Ceres' Occator crater and its faculae explored through geologic mapping. *Icarus* **320**, 7–23 (2018).
16. Scully, J. E. C. et al. Evidence for the interior evolution of Ceres from geologic analysis of fractures. *Geophys. Res. Lett.* **44**, 9564–9572 (2017).
17. Sizemore, H. et al. A global inventory of ice-related morphological features on dwarf planet Ceres: implications for the evolution and current state of the cryosphere. *J. Geophys. Res.* **124**, 1650–1689 (2019).
18. Sori, M. M. et al. The vanishing cryovolcanoes of Ceres. *Geophys. Res. Lett.* **44**, 1243–1250 (2017).
19. Ruesch, O. et al. Cryovolcanism on Ceres. *Science* **353**, aaf4286 (2016).
20. Quick, L. et al. A possible brine reservoir below Occator crater: thermal and compositional evolution and formation of the Cerealia Dome and Vinalia Faculae. *Icarus* **320**, 119–135 (2019).
21. Bland, M. T. et al. Dome formation on Ceres by solid-state flow analogous to terrestrial salt tectonics. *Nat. Geosci.* **12**, 797–801 (2018).
22. Ruesch, O. et al. Slurry extrusion on Ceres from a convective mud-bearing mantle. *Nat. Geosci.* **12**, 505–509 (2019).
23. Castillo-Rogez, J. C. et al. Conditions for the preservations of brines inside Ceres. *Geophys. Res. Lett.* **46**, 1963–1972 (2019).
24. Travis, B. J., Bland, P. A., Feldman, W. C. & Sykes, M. V. Hydrothermal dynamics in a CM-based model of Ceres. *Meteorit. Planet. Sci.* **53**, 2008–2032 (2018).
25. Bowling, T. J. et al. Post-impact thermal structure and cooling timescales of Occator crater on asteroid 1 Ceres. *Icarus* **320**, 110–118 (2019).
26. Hesse, M. & Castillo-Rogez, J. C. Conditions for the long-term preservation of a local brine reservoir below Occator crater on Ceres. *Geophys. Res. Lett.* **46**, 1213–1221 (2018).
27. De Sanctis, M. C. et al. Recent emplacement of hydrated sodium chloride on Ceres from ascending salty fluids. *Nat. Astron.* https://doi.org/10.1038/s41550-020-1138-8 (2020).
28. Castillo-Rogez, J. C. et al. Ceres: astrobiological target and possible ocean world. *Astrobiology* **20**, 269–291 (2020).
29. Neveu, M. & Desch, S. J. Geochemistry, thermal evolution, and cryovolcanism on Ceres with a muddy ice mantle. *Geophys. Res. Lett.* **42**, 10197–10206 (2015).
30. Fagents, S. A. Considerations for effusive cryovolcanism on Europa: the post Galileo perspective. *J. Geophys. Res.* **108**, 5139–5158 (2003).
31. Schenk, P. et al. The central pit and dome at Cerealia Facula bright deposit and floor deposits in Occator crater, Ceres: morphology, comparisons and formation. *Icarus* **320**, 159–187 (2018).
32. Raponi, A. et al. Mineralogy of Occator crater on Ceres and insight into its evolution from the properties of carbonates, phyllosilicates, and chlorides. *Icarus* **320**, 83–96 (2019).
33. Konopliv, A. S. et al. The Ceres gravity field, spin pole, rotation period and orbit from the Dawn radiometric tracking and optical data. *Icarus* **299**, 411–429 (2018).
34. Park, R. S. et al. High-resolution shape model of Ceres from stereophotoclinometry using Dawn imaging data. *Icarus* **319**, 812–827 (2019).
35. Fu, R. R. et al. The interior structure of Ceres as revealed by surface topography. *Earth Planet. Sci. Lett.* **476**, 153–164 (2017).
36. Hager, B. H. & Clayton, R. W. in *Mantle Convection: Plate Tectonics and Global Dynamics. The Fluid Mechanics of Astrophysics and Geophysics* Vol. 4, 657–763 (Gordon and Breach Science Publishers, 1989).
37. Hemingway, D. J. & Matsuyama, I. Isostatic equilibrium in spherical coordinates and implications for crustal thickness on the Moon, Mars, Enceladus, and elsewhere. *Geophys. Res. Lett.* **44**, 7695–7705 (2017).
38. Konopliv, A. S., Banerdt, W. B. & Sjogren, W. L. Venus gravity: 180th degree and order model. *Icarus* **139**, 3–18 (1999).
39. MacKay, D. J. C. *Information Theory, Inference and Learning Algorithms* (Cambridge Univ. Press, 2003).
40. Gregory, P. *Bayesian Logical Data Analysis for the Physical Sciences: A Comparative Approach with Mathematica® Support* (Cambridge University Press, 2005).
41. MacMillan, W. D. *The Theory of the Potential* (Dover Publications, 1930).
42. Goodman, J. & Weare, J. Ensemble samplers with affine invariance. *Commun. Appl. Math. Computat. Sci.* **5**, 65–80 (2010).
43. Collins, G. S., Melosh, H. J. & Ivanov, B. A. Modeling damage and deformation in impact simulations. *Meteorit. Planet. Sci.* **39**, 217–231 (2004).
44. Wünnemann, K., Collins, G. S. & Melosh, H. J. A strain-based porosity model for use in hydrocode simulations of impacts and implications for transient crater growth in porous targets. *Icarus* **180**, 514–527 (2006).
45. Marchi, S. et al. The missing last impact craters on Ceres. *Nat. Commun.* **7**, 12257 (2016).
46. Castillo-Rogez, J. C. et al. Insights into Ceres' evolution from surface composition. *Meteorit. Planet. Sci.* **53**, 1820–1843 (2018).

Author contributions

C.A.R. led the preparation of the manuscript and the geophysical data analysis and interpretation with A.I.E. (MCMC modelling), J.C.C.-R. and M.A.H (thermal modelling), and S.M. and B.C.J. (scaled iSALE results). J.E.C.S. analysed dome morphology, D.L.B., H.G.S. and P.M.S. contributed to geomorphologic interpretation and

Competing interests

The authors declare no competing interests.

Additional information

Extended data is available for this paper at https://doi.org/10.1038/s41550-020-1168-2.
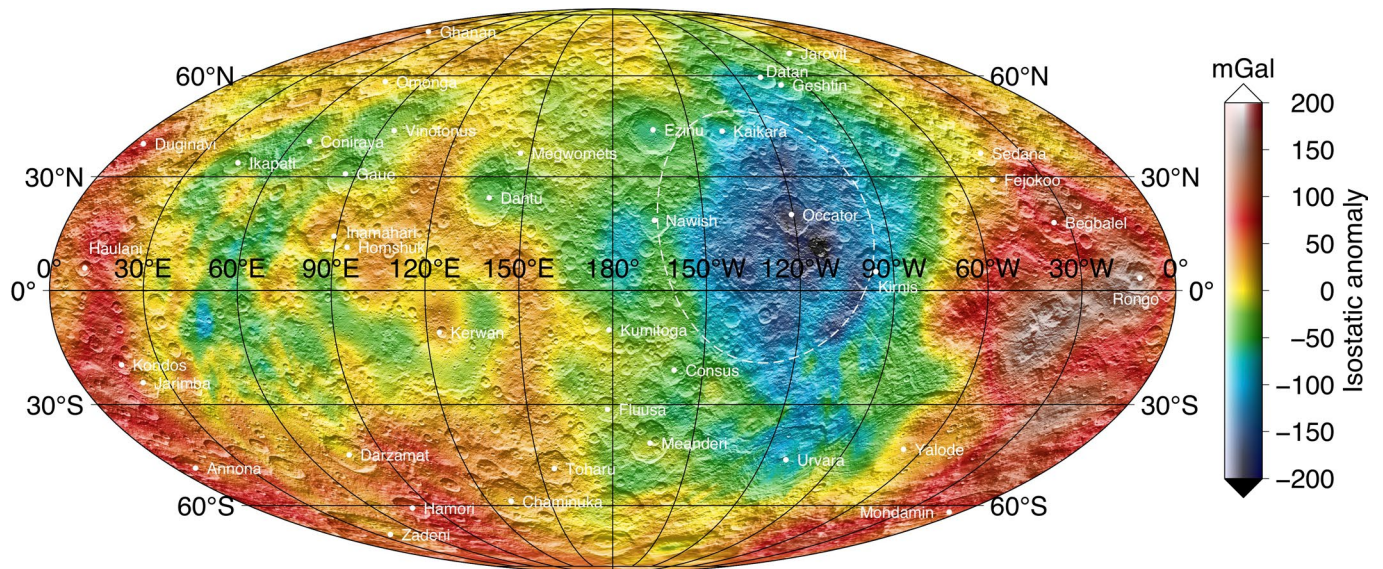
Correspondence and requests for materials should be addressed to C.A.R.

Peer review information *Nature Astronomy* thanks Douglas Hemingway and the other, anonymous, reviewer(s) for their contribution to the peer review of this work.
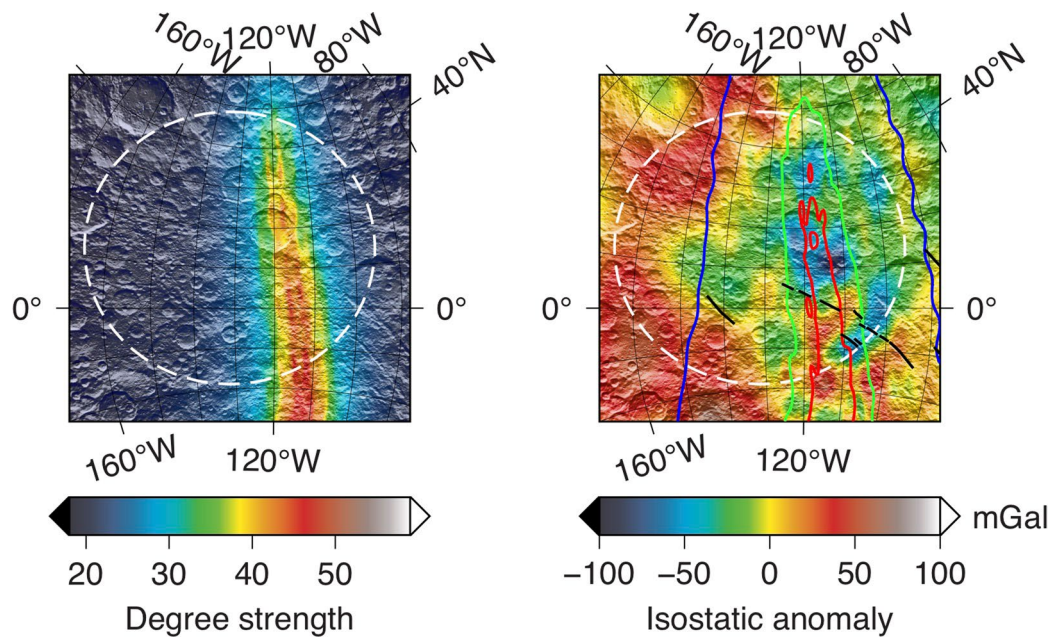
Reprints and permissions information is available at www.nature.com/reprints.

Publisher's note Springer Nature remains neutral with regard to jurisdictional claims in published maps and institutional affiliations.
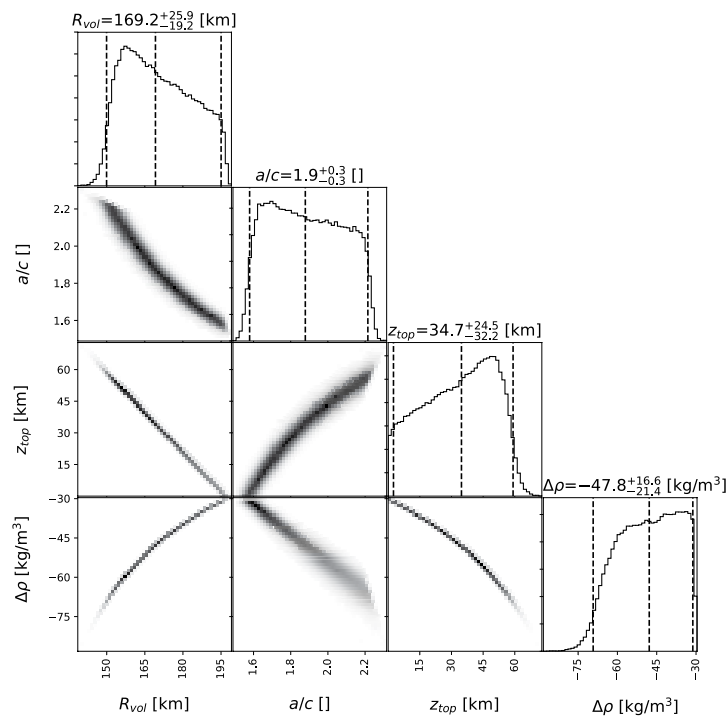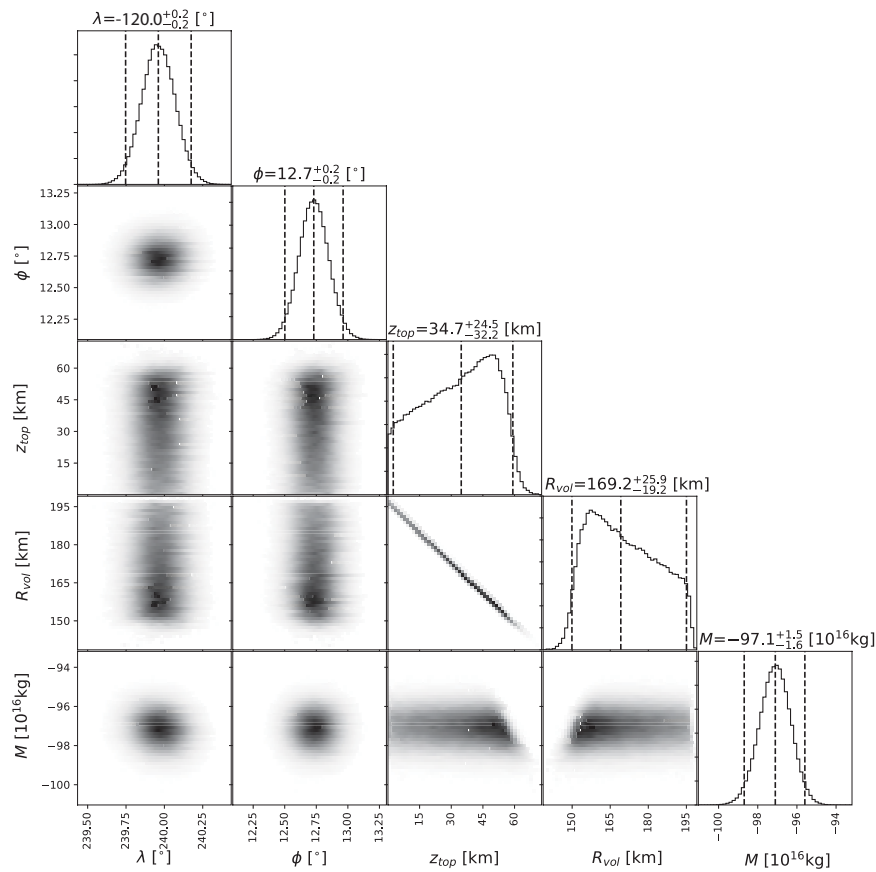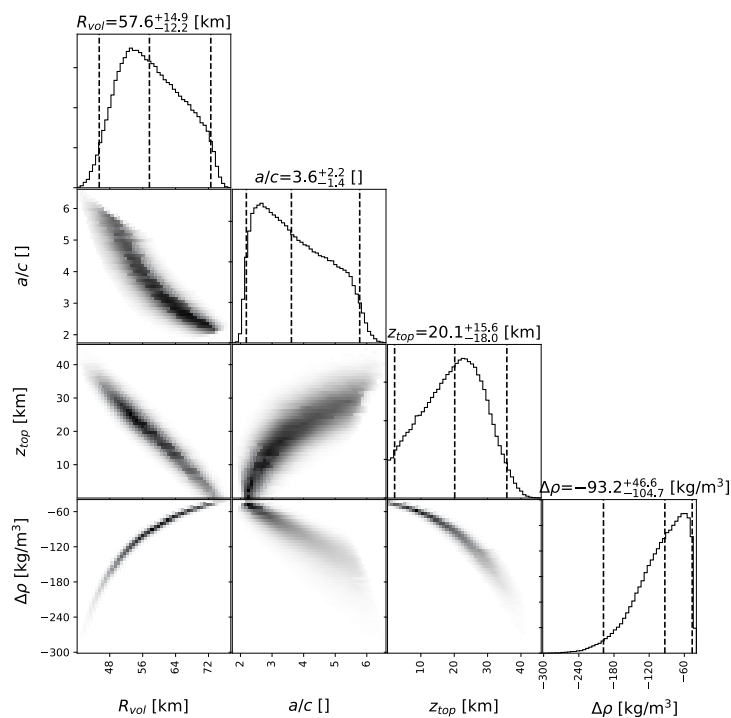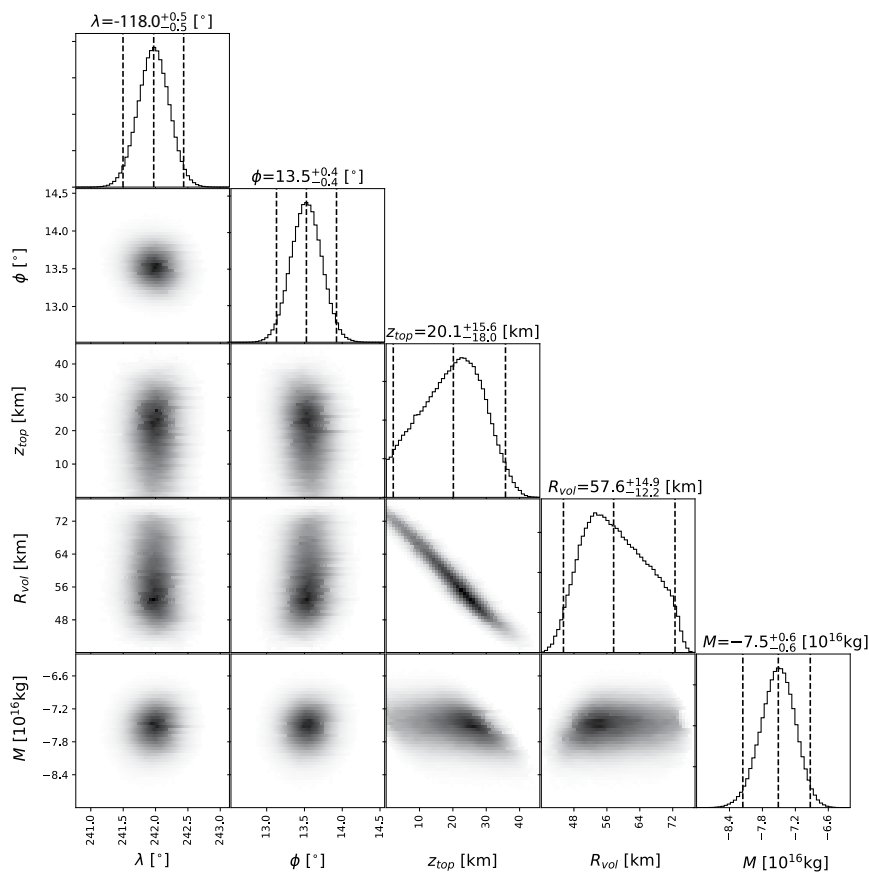
Extended Data Fig. 1 | Isostatic gravity anomaly for degrees n=1 to local degree strength[4] including XM2 high-resolution data. The outline of Hanami Planum in white dashed curve.
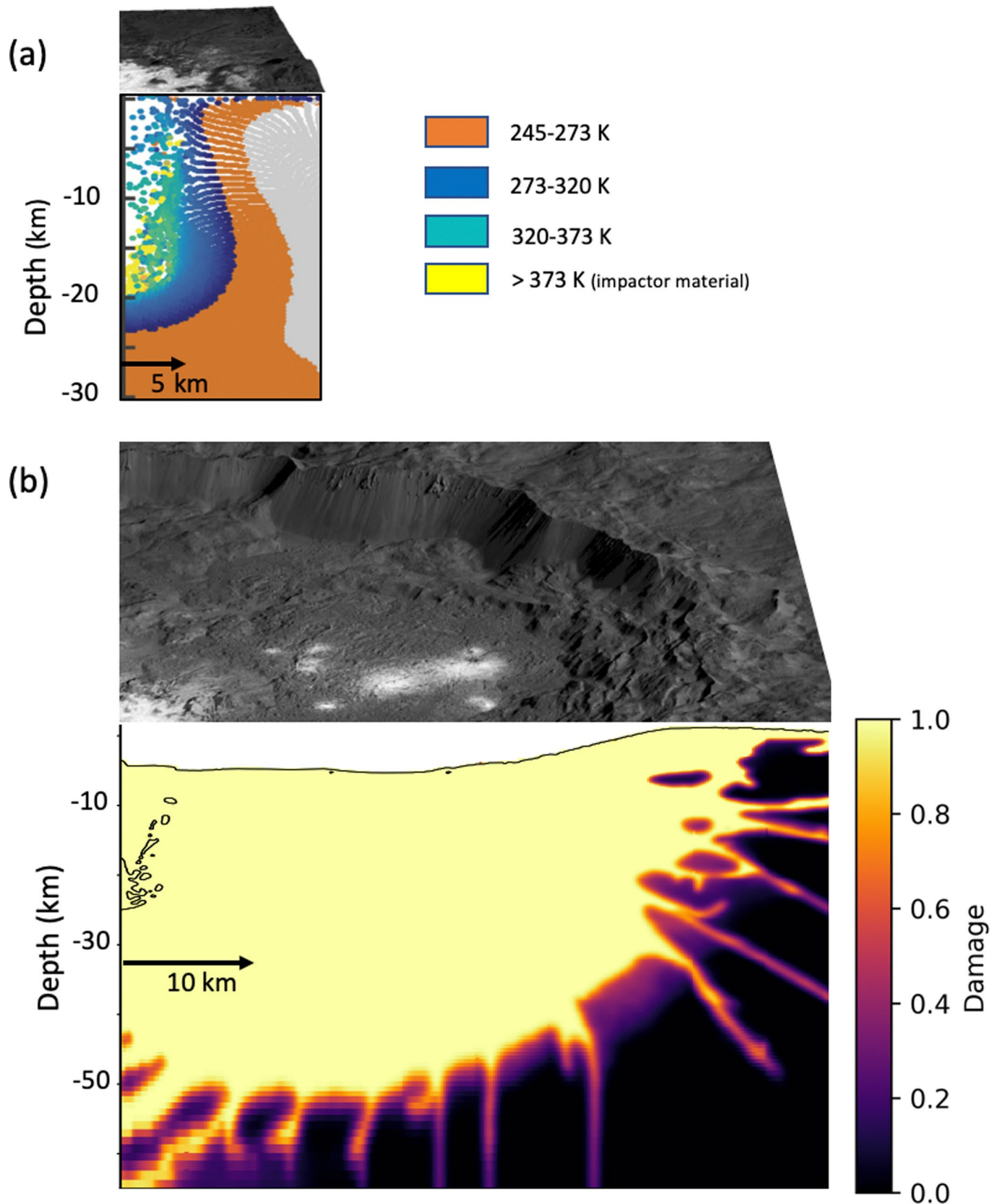
Extended Data Fig. 2 | Degree strength and isostatic anomaly maps through Hanami Planum. The degree strength (left plot) is overplotted over the isostatic anomaly in the right panel. Degree strength equals 20, 30 and 40 for the blue, green and red contours, respectively.
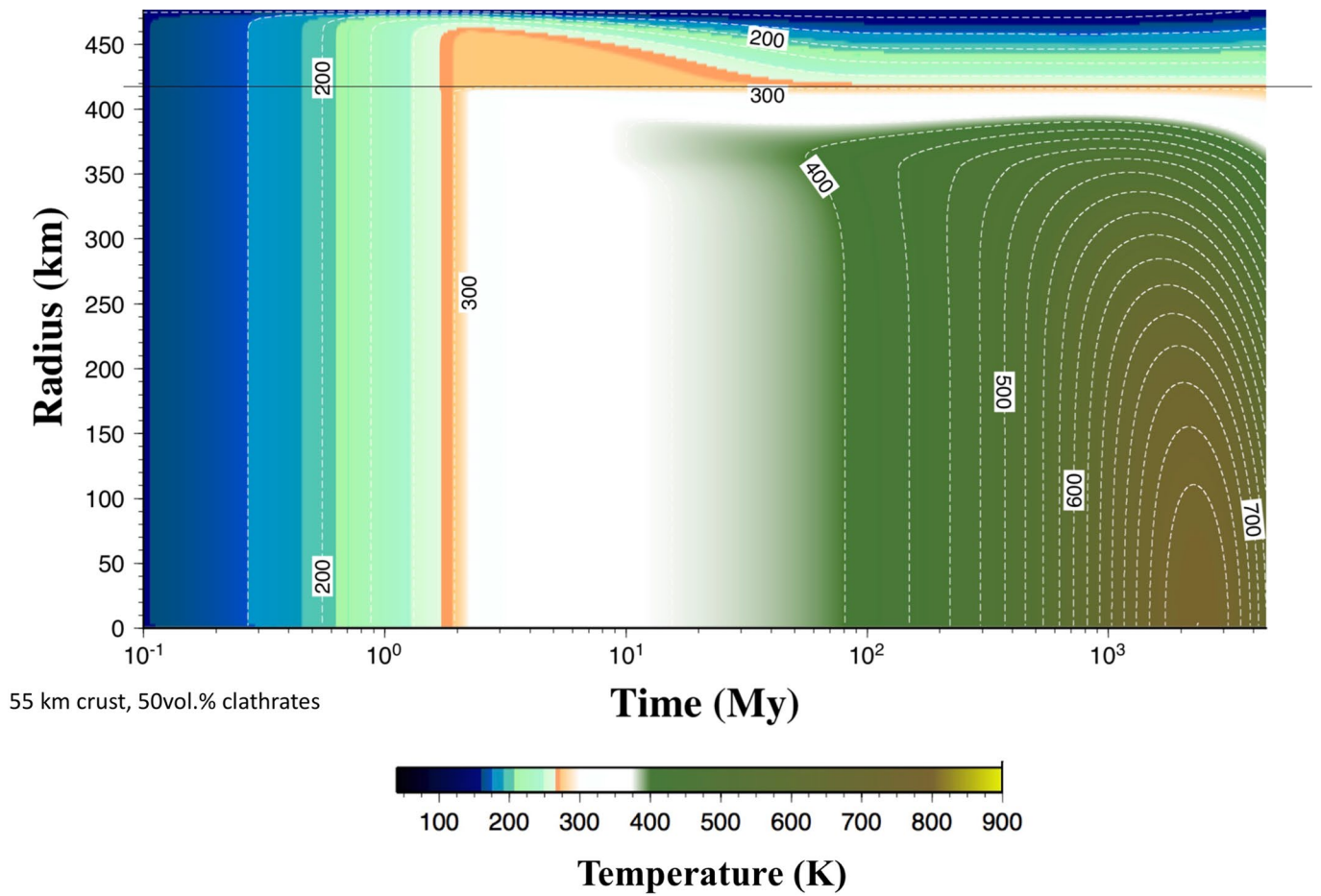
Extended Data Fig. 3 | Posterior distributions resulting from MCMC modeling of gravity field from n=1 to local degree strength beneath Hanami planum. Top: Longitude (λ), latitude (ϕ) and total mass deficit (M) are well-constrained. Bottom: Source aspect ratio (i.e., ratio of horizontal ellipsoid semi-axis a to the vertical semi-axis c), depth to source (Z_{top}) and density contrast ($\Delta\rho$) show broader probable ranges. The 2.5 – 97.5 % confidence intervals are shown on the top of each histogram.

Extended Data Fig. 4 | Posterior distribution resulting from MCMC modeling of gravity field from n=1 to local degree strength beneath the Occator crater region. The average field in an annulus between 20 and 30 degrees from the center of anomaly A was removed to suppress the large long-wavelength negative isostatic anomaly before the inversion was performed. Top: longitude (λ), latitude (ϕ) and total mass deficit (M) are well-constrained. Bottom: Source aspect ratio (i.e., ratio of horizontal ellipsoid semi-axis a to the vertical semi-axis c), depth to source (Z_{top}) and density contrast ($\Delta\rho$) show broader probable ranges. The 2.5 – 97.5 % confidence intervals are shown on the top of each histogram.

Extended Data Fig. 5 | Effect of the impact on the region predicted by hydrocode model. Maps of post-impact temperature field **a**, and damage **b**, with depth. Temperature field was scaled from iSALE hydrocode modelling by[25] using updated thermal evolution models that reflect the current understanding based on Dawn data[23] (See Methods). The damage region plot is from the modeling of[25]. Intact material has a damage parameter, $D=0$, while thoroughly fractured material has $D=1$[43].

55 km crust, 50vol.% clathrates

Extended Data Fig. 6 | Thermal model for the Hanami planum region assuming a thermal gradient of 2.73 K/km. The solid black line at ~420 km indicates the boundary between the ice- and hydrate-rich crust (above) and the rocky mantle (below). See Methods for details.

	a (km)	c (km)	M (10^{16} kg)	λ (°W)	ϕ (°N)	r (km)	$\Delta\rho$ (kg/m³)	z_{top} (km)	z_{bot} (km)
Hanami Planum	$208.9^{+18.8}_{-14.4}$	$111.1^{+32.3}_{-22.6}$	$-97.1^{+1.5}_{-1.6}$	$120.0^{+0.2}_{-0.2}$	$12.7^{+0.2}_{-0.2}$	$334.1^{+3.9}_{-4.1}$	$-47.8^{+16.6}_{-21.4}$	$34.7^{+24.5}_{-32.2}$	$257.0^{+33.3}_{-21.8}$
Occator Region	$88.9^{+8.8}_{-10.2}$	$24.5^{+18.1}_{-10.1}$	$-7.5^{+0.6}_{-0.6}$	$118.0^{+0.5}_{-0.5}$	$13.5^{+0.4}_{-0.4}$	$434.5^{+7.3}_{-8.0}$	$-93.2^{+46.6}_{-104.7}$	$20.1^{+15.6}_{-18.0}$	$69.7^{+20.6}_{-12.0}$

Extended Data Table 1 | Results of MCMC modelling. The median values are given with 2.5th to 97.5th percentile ranges.

parameter [units]	Minimum bound	Maximum bound
horizontal semiaxis [km]	100.0	350.0
vertical semiaxis [km]	75.0	150.0
center longitude [º]	Within 5º of 120.25ºW and 12.75ºN	
center latitude [º]		
center depth [km]	130.0	170.0
density contrast [kg/m^3]	-700.0	0.0

Extended Data Table 2 | Bounds on the model parameters for the Hanami Planum MCMC runs. Lower and upper bounds are given for the semiaxes' lengths, central depth and density contrast of the anomolous ellipsoid. Note that the geographic coordinates of the center of the anomaly were constrained to be within a 5° small circle of the specified location. In addition, the top point on the vertical ellpsoid axis was constrained to be the shallowest point of the anomalous ellipsoid.

parameter [units]	Minimum bound	Maximum bound
horizontal semiaxis [km]	75.0	150.0
vertical semiaxis [km]	2.0	45.0
center longitude [º]	Within 4º of 118.5ºW and 13.4ºN	
center latitude [º]		
center depth [km]	20.0	60.0
density contrast [kg/m^3]	-500.0	0.0

Extended Data Table 3 | Bounds on the model parameters for the Occator SE MCMC runs. Lower and upper bounds are given for the semiaxes' lengths, central depth and density contrast of the anomolous ellipsoid. Note that the geographic coordinates of the center of the anomaly were constrained to be within a 5° small circle of the specified location. In addition, the top point on the vertical ellpsoid axis was constrained to be the shallowest point of the anomalous ellpsoid.

parameter [units]	Hanami Planum	Occator SE
semimajor axis [km]	208.8	88.8
semiminor axis [km]	110.9	24.4
longitude [º]	120.0ºW	118.0ºW
latitude [º]	12.7ºN	13.5ºN
radius from body center [km]	334.1	434.5
density contrast [kg/m³]	-48.0	-93.4

Extended Data Table 4 | **The model parameters for the Hanami Planum and Occator SE representative models shown in Figure 2.** These model parameters represent the median values and do not correspond to the maximum-likelihood solution.